

**SYNTHESIS AND PHOTOELECTROCHEMICAL
CHARACTERIZATION OF HEMATITE BASED
PHOTOANODES AND CFD SIMULATION STUDIES
IN WATER SPLITTING**

SATIRTHA KUMAR SARMA



**DEPARTMENT OF CHEMICAL ENGINEERING
INDIAN INSTITUTE OF TECHNOLOGY DELHI
OCTOBER 2022**

© **Indian Institute of Technology Delhi (IITD), New Delhi, 2022**

**SYNTHESIS AND PHOTOELECTROCHEMICAL
CHARACTERIZATION OF HEMATITE BASED
PHOTOANODES AND CFD SIMULATION STUDIES
IN WATER SPLITTING**

by

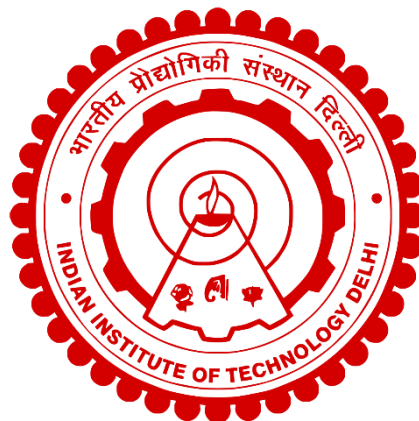
SATIRTHA KUMAR SARMA

Department of Chemical Engineering

Submitted

in fulfilment of the requirements of the degree of Doctor of Philosophy

to the



INDIAN INSTITUTE OF TECHNOLOGY DELHI

OCTOBER 2022

- *This thesis is dedicated to my beloved parents and brother* -

Certificate

This is to certify that the thesis entitled “**Synthesis and Photoelectrochemical Characterization of Hematite Based Photoanodes and CFD Simulation Studies in Water Splitting**” submitted by Mr. Satirtha Kumar Sarma to the Indian Institute of Technology Delhi for the award of the degree of Doctor of Philosophy in Chemical Engineering, is a record of bonafide research work carried out by him. Mr. Satirtha Kumar Sarma has worked under our guidance and supervision and has fulfilled the requirements for the submission of the thesis.

The results contained in this thesis have not been submitted in part or in full to any other university or institute for the award of any degree or diploma.

Prof. Ratan Mohan
Department of Chemical Engineering
Indian Institute of Technology Delhi
India – 110016

Prof. Anupam Shukla
Department of Chemical Engineering
Indian Institute of Technology Delhi
India – 110016

Acknowledgments

Firstly, I would like to express my sincere gratitude to my supervisors Prof. Ratan Mohan and Prof. Anupam Shukla for their continuous support during my Ph.D study and related research. I express my sincere gratitude and indebtedness to them for their guidance, encouragement and fruitful discussions. I am thankful to them for their valuable suggestions and precise corrections to improve all the scientific papers and this Ph.D thesis.

Besides my supervisors, I would like to express my deep sense of gratitude to Prof. Kamal Kishore Pant, Prof. Sreedevi Upadhyayula and Prof. Pravin Ingole for their insightful comments, questions and encouragement, which helped me to widen my research from various perspectives. I would like to acknowledge the great scientific environment as well as infrastructure of IIT Delhi which lead to the completion of this Ph.D thesis. I would like to acknowledge the research facilities (CRF, NRF and CSC) of IIT Delhi, XPS facility of IIT Kanpur, Prof. S. Basu's lab for providing material characterization and simulation facilities. I wish to acknowledge my lab-mates, Mrs. Pooja Jangir, Ms. Isha Atrey, Mr. Rahul Raghuwanshi, Mrs. Mythili Peparthi and Mr. Jayant Nagar for their help and moral support throughout this journey. I also wish to thank my senior Dr. Rupesh Tamgadge for his valuable inputs and help.

Finally, I bow in deep respect and appreciation to my dearest parents, my wife (Nabanita), elder brother (Siddhartha) and entire family members for their encouragement, sacrifice and support in finishing this thesis. Last but not the least, my friends, specially, Aditya, Prasun, Mohit, Aniket, Nitesh, Abinash Da and Amar Sir for their constant support and encouragement through ups and downs of this long journey of Ph.D.

Abstract

Photoelectrochemical (PEC) water splitting is widely regarded as an effective process for sustainable storage of solar energy as chemical energy in the form of H₂. For application in water splitting, pristine and Sn doped (1%, 3% and 5%) hematite nanoparticles were prepared by hydrothermal process. Structural change from nanorods to nanocorals is seen for the Sn doped hematite products. The Sn 3d XPS peak analysis reveals that Sn has been doped into the hematite lattice. Linear Sweep Voltammetry (LSV) and Electrochemical Impedance Spectroscopy (EIS) analysis confirm that 1% Sn doped hematite has the highest photocurrent density (3 mA cm⁻² at 1 V vs. Ag/AgCl) and least charge transfer resistance among the doped products. UV-VIS, Photoluminescence and Mott-Schottky analyses further show that optimum optical and electrical properties are observed for this level of Sn doping. To enhance the PEC performance and study the effect of precursor concentration, NiFe layered double hydroxide (LDH) synthesized in-situ at two different precursor concentrations (low and high) was coated on Sn-doped hematite. A high photocurrent density ca. 2.9 mA cm⁻² at 1.8 V vs. reversible hydrogen electrode (RHE) and a 170 mV cathodic shift in onset potential was recorded for Sn-doped hematite coated with low precursor concentration compared to pristine hematite (0.22 mA cm⁻² at 1.8 V vs. RHE). The enhanced PEC activity can be attributed to the synergistic effect of Sn doping and NiFe-LDH co-catalyst on hematite, which contributes to efficient separation of the photogenerated charge carriers and reduces hole accumulation at the surface. However, for the high precursor concentration case, the formation of a thick film of NiFe-LDH results in a comparatively lower current density (0.85 mA cm⁻² at 1.8 V vs. RHE). The results obtained show that NiFe-LDH can be used as an effective co-catalyst to significantly enhance the charge transport properties of tin-doped hematite. Further, efficient management of the oxygen gas bubbles evolving at the photoanode surface is

important for improving the overall performance of a PEC cell. It is desirable to reduce the bubble residence time at or near the electrode surface for promoting an easy electrolyte access to the photoanode surface, thereby enhancing the oxygen evolution reaction (OER) kinetics. Computational fluid dynamics (CFD) simulation results and experimental investigation show an enhanced bubble rise and improved PEC performance with the application of forced convection. This can be attributed to the fact that a higher bubble rise with increased electrolyte inflow velocity reduces the bubble residence time. Moreover, the CFD simulation study conducted shows a reduced bubble adhesion for hydrophilic hematite nanorod arrays, compared to planar morphology of photoanode due to capillary wicking. The developed model predicts that the detachment of the continuous contact between the adhered bubble and nanorod surface results in a reduced blockage of active sites at the bubble base, thereby enhancing the PEC performance. Experimental investigation reveals a 4-fold increment in photocurrent density and reduction in charge transfer resistance for hematite nanorod arrays, compared to planar morphology electrodes. To address the potential drop problem associated with a scaled up (10 cm × 10 cm) photoanode substrate (FTO), a silver mesh thin film was used. Two different patterned silver mesh configurations (square mesh and fine square) were studied, and the simulation results predict an effective electrode area of 100% for oxygen evolution reaction for both the cases.

सार

प्रकाशिक विद्युत् रसायनिकी (प्र.वि.र.) जल विभाजन को व्यापक रूप से सौर ऊर्जा के स्थायी भंडारण के लिए हाइड्रोजन (H₂) के रूप में रासायनिक ऊर्जा के रूप में एक प्रभावी प्रक्रिया के रूप में माना जाता है। जल विभाजन में आवेदन के लिए, हेमेटाइट और Sn डोपेड (1%, 3% और 5%) हेमेटाइट नैनोकणों को दो-चरण तापन प्रक्रिया के माध्यम से हाइड्रोथर्मल रूप से तैयार किया गया था। Sn डोपेड हेमेटाइट उत्पादों के लिए नैनोरोड्स से नैनोकोरल्स में संरचनात्मक परिवर्तन देखा जाता है। Sn 3d XPS चोटी के विश्लेषण से पता चलता है कि Sn को हेमेटिट लैटिस में डोप हो गया है। लीनियर स्वीप वोल्टामेट्री (LSV) और इलेक्ट्रोकेमिकल इम्पीडेंस स्पेक्ट्रोस्कोपी (EIS) विश्लेषण इस बात की पुष्टि करते हैं कि 1% Sn डोपेड हेमेटाइट में उच्चतम प्रकाशिक धारा घनत्व (3 mA cm⁻² at 1 V vs. Ag/AgCl) है और डोप किए गए उत्पादों के बीच कम से कम चार्ज ट्रांसफर प्रतिरोध है। UV-VIS, Photoluminescence और Mott-Schottky विश्लेषण आगे बताते हैं कि इस उत्पाद के लिए अनुकूलतम ऑप्टिकल और विद्युत गुण देखे गए हैं।

प्र.वि.र के प्रदर्शन को बढ़ाने और अग्रदूत एकाग्रता के प्रभाव का अध्ययन करने के लिए, NiFe के दो अलग-अलग सांद्रता (निम्न और उच्च) पर डबल हाइड्रॉक्साइड (LDH) को Sn डोपेड हेमेटाइट पर लेपित किया था। एक उच्च प्रकाश धारा घनत्व ca. 2.9 mA cm⁻² at 1.8 V vs. RHE और एक 170 mV कैथोडिक बदलाव की शुरुआत की क्षमता की तुलना में हेमेटाइट (0.22 mA cm⁻² at 1.8 V vs. RHE) की तुलना में कम अग्रदूत एकाग्रता के साथ लेपित Sn-डोपेड हेमेटाइट के लिए दर्ज किया गया था। बढ़ी हुई प्र.वि.र गतिविधि को हेमेटाइट पर Sn डोपिंग और NiFe-LDH सह-उत्प्रेरक के सहक्रियात्मक प्रभाव के कारण हो सकता है, जो फोटोजेनरेटेड चार्ज वाहक के कुशल पृथक्करण में योगदान देता है और सतह पर hole accumulation को कम करता है। हालांकि, उच्च अग्रदूत एकाग्रता मामले के लिए, NiFe-LDH की एक मोटी फिल्म के गठन के परिणामस्वरूप तुलनात्मक रूप से कम प्रकाशिक धारा घनत्व (0.85

mA cm⁻² at 1.8 V vs. RHE) होता है। प्राप्त परिणामों से पता चलता है कि NiFe-LDH को Sn-डॉप्ड हेमेटाइट के चार्ज ट्रांसपोर्ट गुणों को बढ़ाने के लिए एक प्रभावी सह-उत्प्रेरक के रूप में इस्तेमाल किया जा सकता है। इसके अलावा, प्र.वि.र सेल के समग्र प्रदर्शन में सुधार के लिए फोटोएनोड सतह पर विकसित होने वाले ऑक्सीजन गैस बुलबुले का कुशल प्रबंधन आवश्यक है। फोटोएनोड सतह पर एक आसान इलेक्ट्रोलाइट पहुंच को बढ़ावा देने के लिए इलेक्ट्रोड सतह पर या उसके पास बुलबुला निवास समय को कम करना वांछनीय है, जिससे ऑक्सीजन विकास प्रतिक्रिया (OER) कैनेटीक्स को बढ़ाया जा सके। कम्प्यूटेशनल तरल गतिकी (CFD) सिमुलेशन परिणाम और प्रयोगात्मक जांच, अधिकृत संवहन के आवेदन के साथ क्रमशः बढ़ी हुई बुलबुला वृद्धि और बेहतर प्र.वि.र प्रदर्शन दिखाते हैं। यह इस तथ्य के लिए जिम्मेदार ठहराया जा सकता है कि बढ़े हुए इलेक्ट्रोलाइट प्रवाह वेग के साथ एक उच्च बुलबुला वृद्धि बुलबुला निवास समय को कम करती है, जिससे प्र.वि.र प्रतिक्रिया में भाग लेने के लिए इलेक्ट्रोड सतह पर इलेक्ट्रोलाइट की आसान पहुंच की अनुमति मिलती है। इसके अलावा, केशिका wicking के कारण फोटोएनोड के तलीय आकारिकी की तुलना में हाइड्रोफिलिक हेमेटाइट नैनोरोड सरणियों के लिए एक कम बुलबुला आसंजन दिखाते हुए कम्प्यूटेशनल तरल गतिकी सिमुलेशन अध्ययन आयोजित किया गया था। विकसित मॉडल बताते हैं कि चिपकने वाले बुलबुले और नैनोरोड सतह के बीच निरंतर संपर्क की टुकड़ी के परिणामस्वरूप बुलबुला आधार पर सक्रिय साइटों की रुकावट कम हो जाती है, जिससे प्र.वि.र प्रदर्शन में वृद्धि होती है। प्रायोगिक जांच से पता चलता है कि इलेक्ट्रोड के प्लेनर आकारिकी की तुलना में प्रकाशिक धारा घनत्व में 4 गुना वृद्धि और हेमेटिट नैनोरोड सरणियों के लिए चार्ज ट्रांसफर प्रतिरोध में कमी आई है। स्केल्ड अप (10 cm × 10 cm) सबस्ट्रेट (FTO) से जुड़ी विद्युत विभव गिरावट समस्या को संबोधित करने के लिए, एक चांदी की जाली वाली पतली फिल्म का उपयोग किया गया था। दो अलग-अलग पैटर्न वाले सिल्वर मेश कॉन्फिगरेशन (स्कायर मेश और फाइन स्कायर) का अध्ययन किया गया था, और सिमुलेशन परिणाम बताते हैं की दोनों मामलों के लिए ऑक्सीजन विकास प्रतिक्रिया के लिए 100% के प्रभावी इलेक्ट्रोड क्षेत्रफल उपलब्ध हैं।

Contents

	Page No.
Abstract	
1 Introduction	1
1.1 Background.....	1
1.2 Photoelectrochemical water splitting process.....	2
1.3 The PEC Cell.....	2
1.4 Materials for water splitting.....	4
1.5 Improving the overall performance.....	6
1.6 Research objectives.....	7
1.7 Organization of thesis.....	7
2 Literature Review	9
2.1 Historical Overview.....	9
2.2 Photoanode materials in water splitting.....	9
2.2.1 Elemental doping on hematite.....	11
2.2.2 Progress in morphology of hematite nanostructures.....	12
2.2.3 Hydrothermal route for synthesis of hematite nanostructures.....	13
2.3 Enhancing the oxygen evolution reaction kinetics.....	13
2.3.1 OER co-catalyst coupling.....	14
2.3.2 Oxygen bubble management.....	17
2.3.2.1 Electrolyte in-flow velocity.....	17
2.3.2.2 Reduce bubble adhesion.....	18
2.3.3 Conductive substrate sheet resistance.....	20
2.4 Summary.....	20
3 Synthesis and Optimization of Sn Dopant Level on Hematite	22
3.1 Introduction.....	22
3.2 Experimental.....	22
3.2.1 Materials.....	22
3.2.2 Synthesis.....	23

	Page No.
3.3 Characterization techniques.....	24
3.4 Results and discussion.....	26
3.4.1 Structural analysis.....	26
3.4.2 Morphology analysis.....	33
3.4.3 Opto-electronic analysis.....	36
3.4.4 Photoelectrochemical characterization.....	39
3.5 Conclusion.....	44
4 NiFe-LDH oxygen evolution reaction co-catalyst loading on Sn:α-Fe₂O₃	45
4.1 Introduction.....	45
4.2 Experimental.....	46
4.2.1 Synthesis of photoanodes.....	46
4.2.2 Material Characterization.....	47
4.2.3 Photoelectrochemical characterization.....	48
4.3 Results and discussion.....	48
4.3.1 Structural analysis from XRD, Raman and XPS.....	48
4.3.2 Morphological changes due to Sn dopant and NiFe-LDH co-catalyst.....	54
4.3.3 Opto-electronic analysis.....	57
4.3.4 Photoelectrochemical analysis.....	59
4.4 Conclusion.....	70
5 CFD Simulation Studies in Water Splitting	72
5.1 Introduction.....	72
5.2 Bubble hydrodynamics effects.....	72
5.2.1 Modeling.....	72
5.2.1.1 Governing equations.....	72
5.2.1.2 Geometries and boundary conditions.....	74
5.2.2 Experimental Section.....	76
5.2.2.1 Materials.....	76
5.2.2.2 Synthesis of hematite nanorod arrays and planar.....	76
5.2.3 Material Characterization.....	77

List of Figures

	Page No.
1.1 A schematic diagram of the PEC cell showing the working (anode), counter (cathode), and reference electrodes along with the reactions at anode and cathode as well as the flow of current in the external circuit.....	3
1.2 A schematic representation of the electron energy levels of semiconductor electrode used for water splitting. The reactions at anode and cathode and the electrochemical potential for the two reactions is also indicated.....	5
1.3 Band edges of some semiconductors for water splitting.....	5
2.1 Schematic showing the role of OER co-catalyst in PEC water splitting.....	15
2.2 Oxygen bubble growth and detachment at various zones at or near photoanode.....	18
2.3 Schematic of Oxygen evolving reaction at Hematite nanorods surface and gas injection into the bubble.....	19
3.1 Material synthesis procedure.....	24
3.2 X-Ray diffraction patterns of (a) Sn0, (b) Sn1, (c) Sn3 and (d) Sn5 samples.....	26
3.3 Hematite (104) and (110) diffraction profiles of Sn0, Sn1, Sn3 and Sn5 samples.....	27
3.4 The W-H analysis of hematite nanoparticles treated at 550 °C.....	29
3.5 Raman spectra of Sn0, Sn1, Sn3 and Sn5 samples.....	30
3.6 (a) XPS full survey scan, (b) XPS spectra of Fe 2p, (c) XPS spectra of Sn 3d and (d) XPS spectra of O 1s.....	31
3.7 EDX spectra of (a) Sn0 (b) Sn1 (c) Sn3 and (d) Sn5.....	32
3.8 SEM images of pristine hematite nanorods sintered at 550 °C, (a) Pristine hematite (scale: 1 μm), (b) Sn 1% doped hematite sample (scale: 1 μm) (Top view), (c) Sn 1% doped hematite sample (scale: 1 μm) (Side view, showing thickness of the prepared layer) (d) Sn 3% doped hematite sample (scale: 1 μm).....	33
3.9 HRTEM imagery of pristine and doped hematite samples i. morphology changes from nanorod for Sn0 (Figure 3.9 (a)) to nanocorals for Sn1 and Sn3 (Figure 3.9 (c) and (e)) ii. SAED pattern for Sn0 (Figure 3.9 (b)), Sn1 (Figure 3.9 (d)) and Sn3 (Figure 3.9 (f)) iii. d spacings from crystal lattice fringes for Sn0 (Figure 3.9 (g)), Sn1 (Figure 3.9 (h) and (i)) and Sn3 (Figure 3.9 (j)).....	36

	Page No.
3.10 UV-VIS plots of pristine and doped hematite nanoparticles.....	37
3.11 Tauc plots of pristine and doped hematite nanoparticles.....	38
3.12 Photoluminescence spectra of pristine and doped products.....	39
3.13 Nyquist plots of doped hematite nanoparticles. Inset: Equivalent circuit for EIS.....	40
3.14 Mott-Schottky plots of pristine and doped hematite nanoparticles.....	42
3.15 LSV plots of pristine and doped hematite nanoparticles.....	43
3.16 Amperometric <i>J-t</i> curve of Sn1 sample for 1200 s of operation.....	43
4.1 Material synthesis procedure for NiFe-LDH coating on Sn:α-Fe ₂ O ₃	47
4.2 XRD patterns of the prepared samples.....	50
4.3 Raman spectra.....	50
4.4 (A) XPS full survey scan of the samples; (B) High resolution XPS fine scanned spectra of (a) Fe 2p for (i) α-Fe ₂ O ₃ , (ii)Sn:α-Fe ₂ O ₃ , (iii)Sn:α-Fe ₂ O ₃ /NiFe(L) and (iv) Sn:α-Fe ₂ O ₃ /NiFe(H), (b) Sn 3d for (i)Sn:α-Fe ₂ O ₃ , (ii)Sn:α-Fe ₂ O ₃ /NiFe(L) and (iii) Sn:α-Fe ₂ O ₃ /NiFe(H), (c) Ni 2p for (i) Sn:α-Fe ₂ O ₃ /NiFe(L) and (ii) Sn:α-Fe ₂ O ₃ /NiFe(H) and (d) O 1s for the prepared samples for (i) α-Fe ₂ O ₃ , (ii) Sn:α-Fe ₂ O ₃ , (iii) Sn:α-Fe ₂ O ₃ /NiFe(L) and (iv) Sn:α-Fe ₂ O ₃ /NiFe(H).....	53
4.5 FESEM images of (a) α-Fe ₂ O ₃ , (b) Sn:α-Fe ₂ O ₃ , (c) Sn:α-Fe ₂ O ₃ /NiFe(L) (Top view) (d) Sn:α-Fe ₂ O ₃ /NiFe(L) (Side view), (e) Sn:α-Fe ₂ O ₃ /NiFe(H) (Top view) (f) Sn:α-Fe ₂ O ₃ /NiFe(H) (Side view) and (g) Image in inset showing magnified side view of Sn:α-Fe ₂ O ₃ /NiFe(H) for the red squared cross-section.....	55
4.6 (a, c, e, j) HRTEM imagery; (b, d, i, l) SAED patterns of α-Fe ₂ O ₃ , Sn:α-Fe ₂ O ₃ , Sn:α-Fe ₂ O ₃ /NiFe(L) and Sn:α-Fe ₂ O ₃ /NiFe(H) respectively; (f) Image in inset showing magnified of NiFe- LDH nanoflake formation on Sn:α-Fe ₂ O ₃ in Sn:α-Fe ₂ O ₃ /NiFe(L); (g, h) Images in inset showing lattice fringes of Sn:α-Fe ₂ O ₃ and NiFe-LDH in Sn:α-Fe ₂ O ₃ /NiFe(L) respectively, and (k) Image in inset shows lattice fringes of NiFe-LDH hexagonal nanoflakes in Sn:α-Fe ₂ O ₃ /NiFe(H).....	56
4.7 (a) UV-vis absorption spectra and (b) Photoluminescence spectra of α-Fe ₂ O ₃ , Sn:α-Fe ₂ O ₃ , Sn:α-Fe ₂ O ₃ /NiFe(L) and Sn:α- Fe ₂ O ₃ /NiFe(H).....	58
4.8 (a) Nyquist plot under solar illumination for α-Fe ₂ O ₃ , Sn:α-Fe ₂ O ₃ , Sn:α-Fe ₂ O ₃ /NiFe(L) and Sn:α-Fe ₂ O ₃ /NiFe(H) at 1.7 V vs. RHE (b) Equivalent circuit model for data fitting and parameters.....	61

4.9 Mott-Schottky plots using the synthesized photoanodes.....	63
4.10 LSVs (Light and Dark) plots using the synthesized photoanodes (b) Chronoamperometric Stability of Sn: α -Fe ₂ O ₃ /NiFe(L).....	65
4.11 Tafel plots for the photoanodes.....	66
4.12 Comparison of the theoretical H ₂ /O ₂ gas evolution and the experimentally generated gas from Sn: α -Fe ₂ O ₃ /NiFe(L) photoanode.....	67
4.13 IPCE plots of Sn: α -Fe ₂ O ₃ and Sn: α -Fe ₂ O ₃ /NiFe(L).....	69
4.14 Proposed charge transfer mechanism of the developed photoanodes used in photoelectrochemical water oxidation.....	70
5.1 Schematic of geometry and mesh for (a) Bubble coalescence study and rise, and (b) morphology dependent bubble adhesion study.....	75
5.2 A schematic of the PEC reactor set-up (a) Light incident from solar simulator, (b) the anode compartment, (c) Membrane, and (d) the cathode compartment.....	78
5.3 (a) Bubble coalescence in bulk electrolyte and (b) Electrolyte flow field affected by bubble rise (m s ⁻¹).....	80
5.4 (a) CFD results using the same initial diameter as Ren et al. (b) Comparison between simulation results and experimental visualization of bubble rise from 0 to 15 ms.....	81
5.5 Steps of coalescence for horizontally placed bubbles (diameter = 0.8 mm and 0.5 mm) with (a) BG = 0.05 mm and $u = 0$ m s ⁻¹ , (b) BG = 0.1 mm and $u = 0$ m s ⁻¹ and (c) BG = 0.05 mm and $u = 0.1$ m s ⁻¹ ; and vertically placed bubbles with (d) BG = 0.05 mm and $u = 0$ m s ⁻¹ , (e) BG = 0.1 mm and $u = 0$ m s ⁻¹ and (f) BG = 0.05 mm and $u = 0.1$ m s ⁻¹	83
5.6 Coalescence and rise for uniformly sized bubbles: (a-c) for $u = 0$ m s ⁻¹ and (d-f) for $u = 0.1$ m s ⁻¹	85
5.7 Electrolyte flow field for uniformly sized bubbles: (a-c) for batch system ($u = 0$ m s ⁻¹) and (d-f) for flow system ($u = 0.1$ m s ⁻¹).....	86
5.8 Bubble detachment and rise profiles with electrolyte inflow velocity (a) 0 m s ⁻¹ , (b) 0.01 m s ⁻¹ , (c) 0.05 m s ⁻¹ and (d) 0.1 m s ⁻¹	87
5.9 Linear Sweep Voltammetry plots of hematite at $u = 0, 0.01, 0.05$ and 0.1 m s ⁻¹	88

	Page No.
5.10 (a) XRD patterns of hematite synthesized hydrothermally and by RF Magnetron sputtering, (b) HR-TEM image (hydrothermally synthesized hematite), (c) lattice fringes (hydrothermally synthesized hematite), and Contact angle by sessile drop method for electrodes with (d) nanorod array and (e) planar morphology.....	90
5.11 Bubble adhesion at: (a, c) hematite nanorod arrays (contact angle = 11.5°), (b) planar surface (contact angle = 55°), and (d) planar surface (contact angle = 11.5°) at time = 0, 0.3, 0.6, 0.9, 1.2 and 1.5 s.....	93
5.12 (a) EIS: Nquist plots of hematite nanorods and planar samples and the fitted equivalent circuit. Inset: Magnified view showing different R_s for the synthesized product, (b) LSV plots of hematite nanorods and planar samples under dark and solar illumination conditions. Inset: FE-SEM images of (i) hematite nanorods and (ii) planar morphology synthesized by hydrothermal and RF magnetron sputtering methods respectively.....	95
5.13 FOM for Au, Ag and Cu as a function of thickness.....	97
5.14 Domain used in simulation showing (a) FTO layer and (b) Pt counter electrode.....	98
5.15 (a) Potential distribution along the FTO film for cell terminal voltage of 3.0 V, (b) The electrode potential variation along a centreline in x direction.....	99
5.16 (a) Potential distribution along the FTO film, using square mesh configuration of silver layer for cell terminal voltage of 3.0 V, (b) The electrode potential variation along a centreline in x direction.....	100
5.17 (a) Potential distribution along the FTO film, using fine square patterned configuration of silver layer for cell terminal voltage of 3.0 V, (b) The electrode potential variation along a centreline in x direction.....	101
A.1 Samples Sn0, Sn1, Sn3 and Sn5 (a) Iron oxy hydroxide (yellow) (b) pristine and doped hematite (red). Annealing the samples at 550 °C for 4 hours resulted in the conversion of β -FeOOH (yellow color) to reddish brown pure hematite.....	107
A.2 (a) Stainless steel hydrothermal autoclave reactor, (b) components of the reactor.....	108
B.1: EDX spectra of (a) Sn: α -Fe ₂ O ₃ /NiFe(L) and (b) Sn: α -Fe ₂ O ₃ /NiFe(H).....	109
B.2: Light harvesting efficiency of Sn: α -Fe ₂ O ₃ , Sn: α -Fe ₂ O ₃ /NiFe(L) and Sn: α -Fe ₂ O ₃ /NiFe(H).....	110
C.1: Bubble hydrodynamics (coalescence and rise profiles) at different inflow velocities ($u = 0.01$ and 0.05 m s^{-1}).....	111

List of Tables

	Page No.
2.1 PEC performance of some hematite based photoanodes.....	16
3.1 Crystallite sizes of pristine and treated products.....	28
3.2 Lattice Strain of pristine and treated samples from Williamson-Hall plot.....	30
3.3 d spacing from Bragg's law and HR-TEM analysis.....	34
3.4 R_s and R_{CT} comparison.....	41
4.1 Elemental composition of the samples.....	52
4.2 Best fit parameters of the equivalent circuit model.....	62
4.3 V_{FB} and N_d of the photoanodes.....	63
4.4 Tafel slopes of doped and co-catalyst loaded samples.....	67
5.1 Physical parameters used for the simulation.....	75
6.1 Comparison of PEC performance.....	105
A.1 Features of the FTO substrate used in experiments.....	107
B.1 Elemental composition of the samples from EDX spectra.....	110

Nomenclature and list of abbreviations

Symbol	Definition	Unit
C	Specific capacitance	F cm ⁻²
C_{bulk}	Capacitance at bulk	F
C_{HL}	Helmholtz layer capacitance	F
D	Crystallite size	nm
d	diameter	nm
E_g	Band Gap	eV
E_{red}°	Standard reduction potential	V
e_0	Electronic charge	C
e^-	Electron	-
G	Interfacial chemical potential	J m ⁻³
g	Acceleration due to gravity	m s ⁻²
h^+	Hole	-
I	Current	mA
J	Photocurrent density	mA cm ⁻²
J_{abs}	Light absorption	-
J_L	Incident irradiance	mW cm ⁻²
K	Scherrer's constant	-
k	Boltzmann Constant	-
N_d	Carrier density	cm ⁻³
p	Pressure	Pa

R_{bulk}	Bulk resistance	Ω
R_{CT}	Charge transfer resistance	Ω
R_S	Series resistance	Ω
T	Transmission	-
T'	Temperature	$^{\circ}\text{C}$
t	Film thickness	nm
V_f	Volume fraction of fluid	-
V_{FB}	Flat band potential	V
z	Number of electrons for releasing one molecule of gas	-
α	Optical absorption coefficient	cm^{-1}
β_{hkl}	Full width half maximum of the main diffraction peaks	radian
λ	Wavelength of Cu-K α radiation	nm
λ'	Mixing energy density	N
θ	Bragg's angle	degree
ϵ	Strain in the sample	-
ν	Frequency of photon	Hz
ϵ	Relative permittivity	F m^{-1}
ϵ_{pf}	Parameter controlling interface thickness	m
ϵ_0	Vacuum permittivity	F m^{-2}
η	Faradaic efficiency	-
η_{inj}	Charge injection efficiency	-
η_{sep}	Charge separation efficiency	-

μ	Viscosity	Ns m^{-2}
ρ	Density	kg m^{-3}
σ	Surface tension coefficient	N m^{-1}
ϕ	Phase field parameter	-
χ	Mobility tuning parameter	m s kg^{-1}
Ψ	Free energy	J m^{-3}
γ	Mobility	-

Abbreviation	Description
AM	Air mass
APCVD	Atmospheric pressure chemical vapor deposition
CB	Conduction band
CFD	Computational fluid dynamics
CPE	Constant Phase Element
CO ₂	Carbon Dioxide
DI	Deionized
EDX	Energy-dispersive X-ray spectroscopy
EIS	Electrochemical Impedance Spectroscopy
FTO	Fluorine doped tin oxide
H ⁺	Hydrogen ion
H ₂	Hydrogen
H ₂ O	Water
HRTEM	High-resolution transmission electron microscope

IPCE	Incident photon to current conversion efficiency
LDA	Laser doppler anemometry
LDH	Layered double hydroxide
LSV	Linear sweep voltammetry
MS	Mott-Schottky
NHE	Normal hydrogen electrode
O ₂	Oxygen
OER	Oxygen evolution reaction
PEC	Photoelectrochemical
PIV	Particle image velocimetry
PL	Photoluminescence
RF	Radio Frequency
RHE	Reversible Hydrogen Electrode
SAED	Selected area (electron) diffraction
SEM	Scanning Electron Microscope
TCF	Transparent conductive film
UV	Ultraviolet
VB	Valence band
XPS	X-ray photoelectron spectroscopy
XRD	X-ray diffraction